Mathematical Modelling and Numerical Analysis Will be set by the publisher
Modélisation Mathématique et Analyse Numérique

INVERSE MODELLING OF IMAGE-BASED PATIENT-SPECIFIC BLOOD VESSELS: ZERO-PRESSURE GEOMETRY AND IN VIVO STRESS INCORPORATION

Joris Bols[1, 2], Joris Degroote[1], Bram Trachet[2], Benedict Verhegghe[2], Patrick Segers[2] and Jan Vierendeels[1]

Abstract. In vivo visualization of cardiovascular structures is possible using medical images. However, one has to realize that the resulting 3D geometries correspond to in vivo conditions. This entails an internal stress state to be present in the in vivo measured geometry of e.g. a blood vessel due to the presence of the blood pressure. In order to correct for this in vivo stress, this paper presents an inverse method to restore the original zero-pressure geometry of a structure, and to recover the in vivo stress field of the final, loaded structure. The proposed backward displacement method is able to solve the inverse problem iteratively using fixed point iterations, but can be significantly accelerated by a quasi-Newton technique in which a least-squares model is used to approximate the inverse of the Jacobian. The here proposed backward displacement method allows for a straightforward implementation of the algorithm in combination with existing structural solvers, even if the structural solver is a black box, as only an update of the coordinates of the mesh needs to be performed.

1991 Mathematics Subject Classification. 65D18,74L15,49Q10,65N21,90C53.

The dates will be set by the publisher.

1. Introduction

In the last decade computational methods, medical imaging techniques and computational power have improved tremendously, leading to an increasing interest in numerical simulations related to the cardiovascular system. Motivations to perform these numerical analyses and – more importantly – to improve their solution methods are (i) to give medical researchers a better comprehension and insight into the pathology of cardiovascular diseases, (ii) to offer them a computational environment allowing to test new and evaluate existing medical procedures and (iii) the general belief that patient-specific computational models will eventually be used in clinical practice.

Nowadays non-invasive imaging techniques such as X-ray computed tomography (CT) and magnetic resonance imaging (MRI) allow for accurate in vivo visualization of 3D patient-specific geometries that are part of the cardiovascular system. The obtained geometries can be completed by flow, wall thickness and wall motion measurements gathered by MRI and/or ultrasound to provide data for patient-specific boundary conditions for

Keywords and phrases: backward displacement method, inverse modelling, image-based modelling, patient-specific blood vessels, in vivo stress, prestress, zero-pressure geometry

[1] Department of Flow, Heat and Combustion Mechanics, Sint-Pietersnieuwstraat 41, B-9000 Ghent, Belgium; e-mail: Joris.Bols@UGent.be

[2] IBiTech-bioMMeda, De Pintelaan 185, B-9000 Ghent, Belgium

the numerical simulations. Together with pressure measurements there is sufficient data available to include patient-specific boundary conditions in computational fluid dynamics (CFD), computational structural dynamics (CSD) and even fluid-structure interaction (FSI) simulations. In CFD models the flow-related measurements can be imposed directly [1] or incorporated into windkessel and/or 1D models [2] at the inlet and outlets. In CSD models the in vivo data can be used to optimize the constitutive law for the tissue material [3] originally obtained by fitting ex vivo measurements. Both models can be coupled to take into account the interaction between the blood flow and the arterial wall in an FSI simulation.

When focusing on the modelling procedure of the arterial system and the arterial wall in particular, it is important to keep in mind that a physiological pressure load is present at the moment of image acquisition and therefore a stress and strain field is present in the in vivo obtained patient-specific geometry. Several authors have shown that neglecting the presence of this physiological pressure load inside blood vessels in general and inside cerebral or aortic aneurysms in particular results in an inaccurate rating of the stresses and deformations [4–8]. As (i) the stress distribution throughout the arterial wall can not be measured and (ii) it is impossible to measure in vivo the zero-pressure geometry of a blood vessel, an inverse problem has to be defined to solve for this geometry or stress field when the in vivo measured geometry and the corresponding internal pressure at the moment of medical imaging are known.

This inverse problem and its solution methods are not only applicable in biomechanical models. There are many engineering applications in which a load free configuration or an initial stress distribution may be useful. For example in production and design processes it can be used to calculate the yet to be manufactured shape of gaskets or rubber seals and even the geometry of the manufacturing tools themselves (e.g. the elastomer puncher in a rubber pad forming process for metal sheets), such that the desired shape is reached under loading conditions [9,10]. Another example can be found in the design process of a turbine blade where the geometrical outcome of a CFD optimization study has to be attained when the blade is subjected to pressure and centrifugal forces [11].

In this paper two methods are presented to solve for the zero-pressure geometry by iteratively updating the nodal coordinates towards the unknown unloaded configuration. Applying the arterial pressure, present at the moment of imaging, in a forward analysis fully recovers the in vivo measured geometry and restores its stress state. This prestressing method allows for a straightforward implementation in combination with existing finite element solvers, even for black box solvers without access to the source code, since only an update of the nodal coordinates is required.

2. Methods

2.1. Problem description

Before defining the inverse problem, a general forward problem is formulated. Therefore, we define a stress free reference configuration by

$$\Omega(\boldsymbol{X}, \boldsymbol{0}) \tag{1}$$

in which $\boldsymbol{X}$ denotes the material coordinates of the undeformed reference geometry, and where the second argument of the configuration Ω refers to the zero stress state that corresponds to this unloaded reference configuration. Then, a forward analysis can be defined as the calculation of the equilibrium configuration

$$\Omega(\boldsymbol{x}, \boldsymbol{\sigma}) \tag{2}$$

with $\boldsymbol{x}$ the coordinates of the deformed geometry and $\boldsymbol{\sigma}$ the second-order stress tensor. As shown in Figure 1, this deformed configuration results from a pressure load p, applied at the inner surface of the undeformed blood vessel wall,

$$p = -\boldsymbol{\tau}.\boldsymbol{n} = -(\boldsymbol{\sigma}.\boldsymbol{n}).\boldsymbol{n}$$

with $\boldsymbol{n}$ the outward unit normal vector, and a zero traction vector ($\boldsymbol{\tau} = \boldsymbol{0}$) at the outer surface of this undeformed reference state (1). Furthermore, the nodes at the ending cross sections of the model in Figure 1 are only allowed

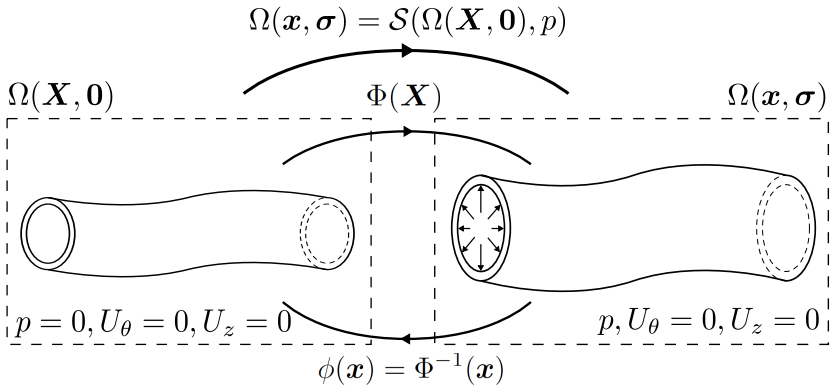

FIGURE 1. Schematic representation and notations of the forward problem.

to move in radial direction with respect to the local centerline

$$\begin{cases} U_\theta = 0 \\ U_z = 0 \end{cases} \tag{3}$$

However, if the axial residual stress has to be taken into account, one can set $U_z \neq 0$ or define an additional axial pressure load.
To be in equilibrium, the equilibrium conditions, the compatibility requirements and the presence of an appropriate material model, which sets the relation between the stress field and the strain field, are satisfied. The equilibrium configuration (2) can be computed by a structural solver, which we denote by $\mathcal{S}$. Using these definitions, we define the forward analysis by

$$\Omega(\boldsymbol{x},\boldsymbol{\sigma}) = \mathcal{S}(\Omega(\boldsymbol{X},\boldsymbol{0}),p) \tag{4}$$

The deformation can be defined by the forward mapping $\Phi : \boldsymbol{X} \mapsto \boldsymbol{x}$ and the deformation gradient tensor $\boldsymbol{F}$

$$\boldsymbol{x} = \Phi(\boldsymbol{X}) \tag{5a}$$

$$\boldsymbol{F} = \frac{\partial \boldsymbol{x}}{\partial \boldsymbol{X}} = \frac{\partial \Phi(\boldsymbol{X})}{\partial \boldsymbol{X}} \tag{5b}$$

The inverse or backward problem calculates the undeformed reference geometry that corresponds to a given geometry, which is deformed due to a pressure load, see Figure 2. Therefore, in contrast to Figure 1, we now assume

$$\begin{cases} \boldsymbol{X} = \boldsymbol{X}^* \\ \boldsymbol{\sigma} = \boldsymbol{\sigma}^* \end{cases}, \qquad \begin{cases} \boldsymbol{x} = \boldsymbol{x}_m \\ p = p_m \end{cases}$$

where $\boldsymbol{X}^*$ and $\boldsymbol{\sigma}^*$ are the zero-pressure geometry present in the undeformed reference configuration and the stress state present in the in vivo configuration, *i.e.* the unknown variables of this inverse problem. The in vivo geometry $\boldsymbol{x}_m$ and the internal pressure load p_m are the known input parameters for the inverse problem, where the subscript m refers to (in vivo) measurements. Then, the backward problem can be formulated as follows: Find the in vivo configuration

$$\Omega(\boldsymbol{x}_m,\boldsymbol{\sigma}^*) \tag{6}$$

which is yet unknown as only $\boldsymbol{x}_m$ is known and $\boldsymbol{\sigma}^*$ is not, and which is in equilibrium with the measured internal pressure load p_m, the zero traction at the outside and the kinematic Dirichlet boundary conditions (3).

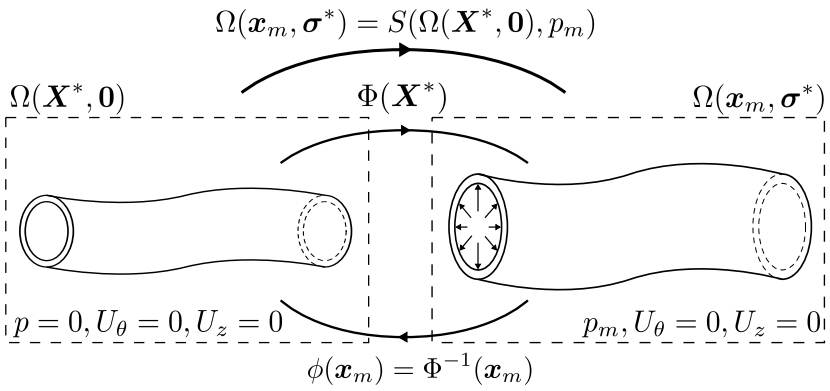

FIGURE 2. Schematic representation and notations for the inverse problem.

Therefore, find the corresponding undeformed reference configuration

$$\Omega(\boldsymbol{X}^*, \mathbf{0}) \tag{7}$$

so that the in vivo equilibrium configuration (6) can be found by imposing the in vivo measured pressure p_m onto the zero-pressure reference configuration (7) in a forward analysis (4)

$$\Omega(\boldsymbol{x}_m, \boldsymbol{\sigma}^*) = S(\Omega(\boldsymbol{X}^*, \mathbf{0}), p_m) \tag{8}$$

Equation (8) results in the stress tensor field $\boldsymbol{\sigma}^*$ which is defined as the *prestress* introduced by the forward analysis or the *in vivo stress* accompanying the in vivo image-based geometry. The unloaded reference geometry can be written as

$$\boldsymbol{X}^* = \phi(\boldsymbol{x}_m) = \Phi^{-1}(\boldsymbol{x}_m)$$

in which $\boldsymbol{\phi} : \boldsymbol{x} \mapsto \boldsymbol{X}$ denotes the inverse deformation mapping. This allows to obtain the original in vivo geometry at the moment of imaging $\boldsymbol{x}_m$ using the in (5a) proposed forward deformation of the zero-pressure geometry $\boldsymbol{X}^*$

$$\Phi(\boldsymbol{X}^*) = \Phi(\phi(\boldsymbol{x}_m)) = \Phi(\Phi^{-1}(\boldsymbol{x}_m)) = \boldsymbol{x}_m$$

2.2. **Backward displacement method**

To solve the backward problem of section 2.1, this paper proposes the backward displacement method (BDM). The method computes the zero-pressure geometry of an in vivo measured structure iteratively by subtracting nodal displacements from the corresponding coordinates of the in vivo measured geometry. These nodal displacements are updated every iteration; they are the result of a forward structural simulation in which the approximation of the zero-pressure geometry is inflated by the in vivo measured pressure. The in vivo stress present in the in vivo measured structure can be calculated by inflating the computed zero-pressure geometry to the in vivo measured pressure. In this paper, the BDM is solved using two numerical methods. The first method proposed in Section 2.2.2 solves the backward displacement problem using fixed point (FP) iterations. The second method presented in Section 2.2.3 accelerates the backward displacement method using a quasi-Newton (QN-ILS) algorithm. Both algorithms make use of a forward structural analysis to update the approximate zero-pressure geometry, evaluating the residual vector as the distance that is still present between the image-based geometry and the geometry resulting from this forward problem. When convergence is reached (i) a zero-pressure geometry is found and (ii) the resulting in vivo measured geometry is recovered and in equilibrium with an in vivo stress field and the in vivo load. Furthermore, only the nodal coordinates of the mesh need to be updated before every iteration, allowing for a straightforward implementation in combination with

existing structural solvers, even if the solver is a black box and no access is granted to the source code (as is the case with most commercial packages).

2.2.1. *Definitions*

The backward displacement function $\mathcal{B}$ is defined as

$$\begin{aligned}\mathcal{B}(\boldsymbol{U}) &= \boldsymbol{x}_m - \boldsymbol{U} \\ &= \tilde{\boldsymbol{X}}\end{aligned} \tag{9}$$

where the output coordinates $\tilde{\boldsymbol{X}} \in \mathbb{R}^{3N\times 1}$ are found by subtracting a displacement variable $\boldsymbol{U} \in \mathbb{R}^{3N\times 1}$ from the in vivo measured geometry $\boldsymbol{x}_m \in \mathbb{R}^{3N\times 1}$. With N the total number of nodes in the three dimensional model, the variables are represented by column vectors as this notation is required for the quasi-Newton formulation of Section 2.2.3.

The structural solver was introduced in Equation (4) by the function $\mathcal{S}(\Omega, p)$ to emphasize that the solver can be treated as a black box. When one is interested in the displacement resulting from the forward analysis (4) in which all input variables except for the coordinates of the reference geometry $\boldsymbol{X} \in \mathbb{R}^{3N\times 1}$ are known, we can define the displacement output of the structural solver by the function $\mathcal{S}_U$

$$\begin{aligned}\mathcal{S}_U(\boldsymbol{X}) &= \boldsymbol{x} - \boldsymbol{X} = \mathcal{S}(\Omega(\boldsymbol{X}, \boldsymbol{0}), p_m) - \boldsymbol{X} \\ &= \boldsymbol{U}\end{aligned} \tag{10}$$

The by $\boldsymbol{x} \in \mathbb{R}^{3N\times 1}$ represented deformed geometry, and thus the nodal displacement output $\boldsymbol{U} \in \mathbb{R}^{3N\times 1}$ of the function $\mathcal{S}_U$ can be found by solving the forward structural problem (4).

Using these definitions, the inverse problem can be described by

$$\tilde{\boldsymbol{X}} = \mathcal{B}(\mathcal{S}_U(\boldsymbol{X})) \tag{11}$$

where a tilde was introduced to distinguish between the output variable of $\mathcal{B}(\mathcal{S}_U)$ and its input variable, as both are in general not the same. However, when the backward problem of Section 2.1 has been solved, Equation (8) has to be satisfied, *i.e.* a forward analysis of the zero-pressure reference configuration $\Omega(\boldsymbol{X}^*, \boldsymbol{0})$ has to result in the in vivo configuration $\Omega(\boldsymbol{x}_m, \boldsymbol{\sigma}^*)$ when applying the internal pressure load p_m present during medical imaging. When this constraint is met, Equation (11) yields the fixed point problem

$$\tilde{\boldsymbol{X}} = \boldsymbol{X} = \boldsymbol{X}^* \tag{12}$$

with $\boldsymbol{X}^* \in \mathbb{R}^{3N\times 1}$ the final zero-pressure geometry. The prestress tensor $\boldsymbol{\sigma}^*$ results from the same forward analysis and can be used as an initial stress tensor in consecutive simulations. The corresponding root finding formulation can be described by

$$\mathcal{R}_X(\boldsymbol{X}) = \mathcal{B}(\mathcal{S}_U(\boldsymbol{X})) - \boldsymbol{X} = \tilde{\boldsymbol{X}} - \boldsymbol{X} = \boldsymbol{0} \tag{13}$$

with $\mathcal{R}_X$ the residual operator in function of the unloaded material coordinates.

2.2.2. *Fixed point strategy*

Equations (11) and (12) suggest that a backward displacement method based on fixed point iterations can be used to solve for the zero-pressure geometry. The fixed point algorithm to recover this zero-pressure geometry and the in vivo stress tensor field is shown in Algorithm 2.1. It starts by initializing an approximation for the zero-pressure geometry $\boldsymbol{X}^{i=0}$. As initial guess, the original image-based geometry $\boldsymbol{x}_m$ is chosen. Then, a fixed point based iterative procedure is performed until convergence is reached. First, the structural solver calculates an equilibrium configuration $\Omega(\boldsymbol{x}^i, \boldsymbol{\sigma}^i)$ from the intermediate reference configuration $\Omega(\boldsymbol{X}^i, \boldsymbol{0})$ loaded with the

full in vivo pressure load p_m. The displacements of the material points in the forward analysis are denoted by $\boldsymbol{U}^i$. Afterwards, the approximation of the zero-pressure geometry ($\boldsymbol{X}^i$) is updated by subtracting the nodal displacements $\boldsymbol{U}^i$ from the *original* image-based coordinates $\boldsymbol{x}_m$. Finally, this procedure leads to an update of the mesh $\boldsymbol{X}^{i+1} = \tilde{\boldsymbol{X}}^i$ used in the next iteration (step 13 in Algorithm 2.1) or, if convergence is reached, to the zero-pressure geometry $\boldsymbol{X}^*$. Furthermore, the forward analysis calculates the stress state $\boldsymbol{\sigma}^i$ (step 9 in Algorithm 2.1) which is left unused throughout the algorithm but represents the in vivo stress tensor $\boldsymbol{\sigma}^*$ present in the in vivo measured geometry upon convergence. During the iterative process, a residual vector $\boldsymbol{r}^i \in \mathbb{R}^{3N\times 1}$ is calculated

$$\boldsymbol{r}^i = \tilde{\boldsymbol{X}}^i - \boldsymbol{X}^i = (\boldsymbol{x}_m - \boldsymbol{U}^i) - \boldsymbol{X}^i \tag{14a}$$

$$= \boldsymbol{x}_m - (\boldsymbol{x}^i - \boldsymbol{X}^i) - \boldsymbol{X}^i \tag{14b}$$

$$= \boldsymbol{x}_m - \boldsymbol{x}^i \tag{14c}$$

This residual vector is a measure for the distances that are still present between the image-based geometry and the deformed geometry resulting from the i^{th} forward analysis. Convergence is reached when the relative residual

$$r^i_{rel} = \frac{\|\boldsymbol{r}^i\|_2}{\|\boldsymbol{r}^0\|_2} < \epsilon \tag{15}$$

is smaller than the convergence criterion ϵ. Where $\|\boldsymbol{r}^i\|_2$ stands for the L^2-norm of the residual vector in the i^{th} iteration.

Algorithm 2.1 (FP BDM)**.** *Fixed point algorithm to recover the zero-pressure geometry and the in vivo stress tensor field.*

1: $i = 0$
2: *Initialize* $\boldsymbol{X}^0 = \boldsymbol{x}_m$
3: $\boldsymbol{U}^0 = \mathcal{S}_U(\boldsymbol{X}^0)$
4: $\tilde{\boldsymbol{X}}^0 = \mathcal{B}(\boldsymbol{U}^0)$
5: $\boldsymbol{r}^0 = \tilde{\boldsymbol{X}}^0 - \boldsymbol{X}^0$
6: $\boldsymbol{X}^1 = \boldsymbol{X}^0 + \boldsymbol{r}^0 = \tilde{\boldsymbol{X}}^0$
7: ***while*** $r^i_{rel} \geq \epsilon$ ***do***
8: $\quad i = i + 1$
9: $\quad \Omega(\boldsymbol{x}^i, \boldsymbol{\sigma}^i) = \mathcal{S}(\Omega(\boldsymbol{X}^i, \boldsymbol{0}), p_m)$
10: $\quad \boldsymbol{U}^i = \mathcal{S}_U(\boldsymbol{X}^i) = \boldsymbol{x}^i - \boldsymbol{X}^i$
11: $\quad \tilde{\boldsymbol{X}}^i = \mathcal{B}(\boldsymbol{U}^i) = \boldsymbol{x}_m - \boldsymbol{U}^i$
12: $\quad \boldsymbol{r}^i = \tilde{\boldsymbol{X}}^i - \boldsymbol{X}^i$
13: $\quad \boldsymbol{X}^{i+1} = \boldsymbol{X}^i + \boldsymbol{r}^i = \tilde{\boldsymbol{X}}^i$
14: ***end while***
15: *Zero-pressure reference geometry* $\boldsymbol{X}^* = \boldsymbol{X}^i$
16: *In vivo stress tensor for the in vivo measured geometry* $\boldsymbol{\sigma}^* = \boldsymbol{\sigma}^i$

2.2.3. *Quasi-Newton strategy with an approximation of the Jacobian's inverse from a least-squares model*

To accelerate the convergence of the backward displacement method, a quasi-Newton iterative method with an approximation for the inverse of the Jacobian from a least-squares model (QN-ILS) can be used. This method uses similar principles as the QN-LS method in which the Jacobian is approximated from a least-squares model and then inverted. The QN-LS method was analyzed for linear problems by Haelterman et al. [12]. The interface quasi-Newton method with an approximation of the inverse of the Jacobian from a least-squares model (IQN-ILS) was introduced by Degroote et al. [13] to couple the interface variables of the flow solver and the structural solver in a partitioned fluid-structure interaction simulation. This method was also analyzed for linear problems by Haelterman et al. [14] in a more general framework, where the method was called QN-ILS. In this paper we

also call the method QN-ILS as the position is computed for all material points and not only for those lying on the interface. The implementation for a nonlinear problem with black box solvers and with the least-squares QR-factorization is as described in [13] and has proven to need less (coupling) iterations compared with other schemes such as Aitken relaxation and Interface-GMRES(R) [15].

The root finding problem described by Equation (13) can be solved using Newton-Raphson iterations. By writing the Jacobian matrix of the residual operator $\mathcal{R}_X$ as

$$\frac{d\mathcal{R}_X}{d\boldsymbol{X}} = \boldsymbol{\mathcal{J}}_X$$

the equations that have to be solved are given by

$$\boldsymbol{\mathcal{J}}_X|_{\boldsymbol{X}^i}\,\Delta\boldsymbol{X}^i = -\boldsymbol{r}^i \tag{16a}$$

$$\boldsymbol{X}^{i+1} = \boldsymbol{X}^i + \Delta\boldsymbol{X}^i \tag{16b}$$

with the i^{th} residual vector, as shown in Equation (14), calculated by

$$\boldsymbol{r}^i = \mathcal{R}_X(\boldsymbol{X}^i) = \mathcal{B}(\mathcal{S}_U(\boldsymbol{X}^i)) - \boldsymbol{X}^i = \tilde{\boldsymbol{X}}^i - \boldsymbol{X}^i \tag{17}$$

Convergence of the Newton-Raphson iterations is reached when the relative residual satisfies Equation (15).

Unlike what happens using the fixed point iterative procedure, the values for $\mathcal{B}(\mathcal{S}_U(\boldsymbol{X}^i))$ are not passed on to the next backward displacement iteration. $\boldsymbol{X}^{i+1}$ gets computed instead using Equation (16a)

$$\Delta\boldsymbol{X}^i = \widehat{\boldsymbol{\mathcal{J}}_X{}^{-1}}\Big|_{\boldsymbol{X}^i}\,(-\boldsymbol{r}^i) \tag{18}$$

in which the hat indicates an approximation. However, the exact Jacobian of $\mathcal{R}_X$ is unknown as we do not know the Jacobian of $\mathcal{S}$. We will now go into more detail on how the product of this approximation for the inverse of the Jacobian with the vector $-\boldsymbol{r}^i$ can be calculated, making use of information obtained during previous backward displacement iterations.

$\Delta\boldsymbol{r}^i = \boldsymbol{0} - \boldsymbol{r}^i$ represents the difference between the desired residual vector and the current one. $\Delta\boldsymbol{r}^i$ is approximated by a linear combination of the known $\delta\boldsymbol{r}^j \in \mathbb{R}^{3N\times 1}$ (for $j = 0, ..., i-1$)

$$\Delta\boldsymbol{r}^i \approx \boldsymbol{V}^i\boldsymbol{c}^i \tag{19}$$

with $\boldsymbol{c}^i \in \mathbb{R}^{i\times 1}$ the coefficients of the decomposition in iteration i and a matrix $\boldsymbol{V}^i \in \mathbb{R}^{3N\times i}$

$$\boldsymbol{V}^i = [\delta\boldsymbol{r}^{i-1}\ \delta\boldsymbol{r}^{i-2}\ \dots\ \delta\boldsymbol{r}^1\ \delta\boldsymbol{r}^0] \tag{20a}$$

$$\delta\boldsymbol{r}^j = \boldsymbol{r}^{j+1} - \boldsymbol{r}^j \qquad (j = 0, \cdots, i-1) \tag{20b}$$

Then, the assumption is made that $\Delta\tilde{\boldsymbol{X}}^i$, corresponding to $\Delta\boldsymbol{r}^i$, can be written by the same linear combination of the, in previous iterations, computed $\delta\tilde{\boldsymbol{X}}^j \in \mathbb{R}^{3N\times 1}$ (for $j = 0, ..., i-1$)

$$\Delta\tilde{\boldsymbol{X}}^i = \boldsymbol{W}^i\boldsymbol{c}^i \tag{21}$$

with a matrix $\boldsymbol{W}^i \in \mathbb{R}^{3N\times i}$

$$\boldsymbol{W}^i = [\delta\tilde{\boldsymbol{X}}^{i-1}\ \delta\tilde{\boldsymbol{X}}^{i-2}\ \dots\ \delta\tilde{\boldsymbol{X}}^{1}\ \delta\tilde{\boldsymbol{X}}^{0}] \tag{22a}$$

$$\delta\tilde{\boldsymbol{X}}^j = \tilde{\boldsymbol{X}}^{j+1} - \tilde{\boldsymbol{X}}^j \quad (j = 0, \cdots, i-1) \tag{22b}$$

Both $\boldsymbol{V}^i$ and $\boldsymbol{W}^i$ are updated at each iteration by the difference between the vectors from the current iteration ($\boldsymbol{r}^i$ and $\tilde{\boldsymbol{X}}^i$) and the vectors from the previous iteration ($\boldsymbol{r}^i$ and $\tilde{\boldsymbol{X}}^i$). Remark that if the tildes would be omitted in Equations (21) and (22), $\Delta\boldsymbol{X}^i(=\boldsymbol{W}^i\boldsymbol{c}^i)$ would become a linear combination of the previously calculated $\delta\boldsymbol{X}^j(j = 0, \cdots, i-1)$, with as result that the rank of $\boldsymbol{W}^{i+1}$ will be the same as the rank of $\boldsymbol{W}^i$. This means that the rank of the matrices $\boldsymbol{W}^i$ would always be equal to one, what would prohibit the convergence of the method since then the rank of the approximation of the inverse of the Jacobian will also become at maximum one. However, for a linear system it has been proven that the use of Equations (21) and (22) returns an exact Jacobian – and thus a converged result – in at most n+1 iterations, with n the number of degrees of freedom of the problem [14]. Remark, however, that in practical applications the convergence rate is much higher.

Considering that the number of columns in $\boldsymbol{V}^i$ is generally much smaller than the number of rows, determined by the number of nodes in the mesh times the spatial dimension of the problem, Equation (19) is an overdetermined system with respect to the elements of $\boldsymbol{c}^i$. Hence, the residual $\Delta\boldsymbol{r}^i = -\boldsymbol{r}^i$ is decomposed as a linear combination of the set of $\Delta\boldsymbol{r}^j = \boldsymbol{r}^{j+1} - \boldsymbol{r}^j$ (for $j = 0, ..., i-1$) by solving the least-squares problem

$$\boldsymbol{c}^i = \arg\min_{\boldsymbol{c}^i} \|\Delta\boldsymbol{r}^i - \boldsymbol{V}^i\boldsymbol{c}^i\|_2 \tag{23}$$

The coefficients of the decomposition, $\boldsymbol{c}^i$, are given by the normal equations

$$\boldsymbol{c}^i = (\boldsymbol{V}^{i^T}\boldsymbol{V}^i)\boldsymbol{V}^{i^T}\Delta\boldsymbol{r}^i \tag{24}$$

However, to be less sensitive to rounding errors introduced during the computations, the least-squares problem is solved by a so-called economy size QR-decomposition of $\boldsymbol{V}^i$

$$\boldsymbol{V}^i = \boldsymbol{Q}^i\boldsymbol{R}^i$$

with $\boldsymbol{Q}^i \in \mathbb{R}^{3N\times i}$ an orthogonal matrix and $\boldsymbol{R}^i \in \mathbb{R}^{i\times i}$ an upper triangular matrix. Because both matrices $\boldsymbol{V}^i$ and $\boldsymbol{W}^i$ are updated at each quasi-Newton iteration the QR-decomposition has to be recalculated. Nevertheless, the cost of the QR-factorization is small compared to the cost of one forward calculation performed by the structural solver $\mathcal{S}_U(\boldsymbol{X}^i)$.

The coefficients of the decomposition $\boldsymbol{c}^i$ are then calculated by solving the triangular system

$$\boldsymbol{R}^i\boldsymbol{c}^i = \boldsymbol{Q}^{i^T}\Delta\boldsymbol{r}^i \tag{25}$$

Using Equation (17), $\Delta\boldsymbol{r}^i$ can be written as

$$\Delta\boldsymbol{r}^i = \Delta\tilde{\boldsymbol{X}}^i - \Delta\boldsymbol{X}^i$$

Substitution of $\Delta\tilde{\boldsymbol{X}}^i$ by Equation (21) and then $\boldsymbol{c}^i$ by Equation (25) results in

$$\Delta\boldsymbol{X}^i = \boldsymbol{W}^i\boldsymbol{c}^i - \Delta\boldsymbol{r}^i \tag{26a}$$

$$= \left(\boldsymbol{W}^i(\boldsymbol{R}^i)^{-1}\boldsymbol{Q}^{i^T} - \boldsymbol{I}\right)\Delta\boldsymbol{r}^i \tag{26b}$$

with $\boldsymbol{I}$ the unity matrix. Identification of Equation (26b) with Equation (18) shows that the approximation of the inverse of the Jacobian can be calculated by

$$\widehat{\mathcal{J}_X{}^{-1}}\Big|_{\boldsymbol{X}^i} = \boldsymbol{W}^i(\boldsymbol{R}^i)^{-1}\boldsymbol{Q}^{iT} - \boldsymbol{I} \tag{27}$$

However, the matrix $\widehat{\mathcal{J}_X{}^{-1}}\Big|_{\boldsymbol{X}^i}$ is never calculated nor stored, but the matrix vector product of $\widehat{\mathcal{J}_X{}^{-1}}\Big|_{\boldsymbol{X}^i}$ with $\Delta\boldsymbol{r}^i$ is computed directly from the calculated coefficients $\boldsymbol{c}^i$, the matrix $\boldsymbol{W}^i$ and the residual vector $\boldsymbol{r}^i$

$$\begin{aligned}\boldsymbol{X}^{i+1} &= \boldsymbol{X}^i + \widehat{\mathcal{J}_X{}^{-1}}\Big|_{\boldsymbol{X}^i}(-\boldsymbol{r}^i)\\ &= \boldsymbol{X}^i + \boldsymbol{W}^i\boldsymbol{c}^i + \boldsymbol{r}^i\end{aligned}$$

so that the required storage for the method is very limited and the calculation time is negligible.

It can be demonstrated that quasi-Newton iterations are performed for the part of $\Delta\boldsymbol{r}^i$ in the span of the columns of $\boldsymbol{V}^i$ (Proposition 2.2) and that fixed point iterations are performed for the part of $\Delta\boldsymbol{r}^i$ orthogonal to the span of the columns of $\boldsymbol{V}^i$ (Proposition 2.3). Algorithm 2.4 shows the complete QN-ILS technique to recover the zero-pressure geometry $\boldsymbol{X}^*$ and to find the in vivo stress $\boldsymbol{\sigma}^*$.

Proposition 2.2. *Quasi-Newton iterations are performed for the part of $\Delta\boldsymbol{r}^i$ in the column span of $\boldsymbol{V}^i$*

Proof. Let $\Delta\boldsymbol{r}^i$ be an element of the column span of $\boldsymbol{V}^i = [\Delta\boldsymbol{r}^{i-1} \dots\ \Delta\boldsymbol{r}^1\ \Delta\boldsymbol{r}^0]$

$$\Delta\boldsymbol{r}^i = \sum_{j=0}^{i-1}\alpha_j\Delta\boldsymbol{r}^j$$

with α_j the coefficients of the linear combination. Then, the components of the decomposition in iteration i, Equations (19) and (21), are given by

$$\boldsymbol{c}^i = \arg\min_{\boldsymbol{c}^i}\|\Delta\boldsymbol{r}^i - \boldsymbol{V}^i\boldsymbol{c}^i\|_2 = [\alpha_{i-1}\ \dots\ \alpha_1\ \alpha_0]^T$$

Equation (26a) can then be reformulated using Equations (20b), (22b) and (17)

$$\begin{aligned}
\Delta \boldsymbol{X}^i = \widehat{\mathcal{J}^{-1}}\Big|_{\boldsymbol{X}^i} \Delta \boldsymbol{r}^i &= \boldsymbol{W}^i \boldsymbol{c}^i - \Delta \boldsymbol{r}^i \\
&= \sum_{j=0}^{i-1} \Delta \tilde{\boldsymbol{X}}^j c_j^i - \sum_{j=0}^{i-1} \alpha_j \Delta \boldsymbol{r}^j \\
&= \sum_{j=0}^{i-1} \left((\tilde{\boldsymbol{X}}^{j+1} - \tilde{\boldsymbol{X}}^j)\, c_j^i - \alpha_j (\boldsymbol{r}^{j+1} - \boldsymbol{r}^j) \right) \\
&= \sum_{j=0}^{i-1} \left((\tilde{\boldsymbol{X}}^{j+1} - \tilde{\boldsymbol{X}}^j)\, \alpha_j - \alpha_j \left((\tilde{\boldsymbol{X}}^{j+1} - \boldsymbol{X}^{j+1}) - (\tilde{\boldsymbol{X}}^j - \boldsymbol{X}^j) \right) \right) \\
&= \sum_{j=0}^{i-1} \alpha_j (\boldsymbol{X}^{j+1} - \boldsymbol{X}^j) \\
&= \sum_{j=0}^{i-1} \alpha_j \Delta \boldsymbol{X}^j
\end{aligned}$$

Thus, iteration i ends up as a quasi-Newton iteration in which the product of the Jacobian's inverse with the vector $\Delta \boldsymbol{r}^i$ can be calculated by a linear combination of known finite differences $\Delta \boldsymbol{X}^j$ (with $j = 0, ..., i-1$). □

Proposition 2.3. *Fixed point iterations are performed for the part of $\Delta \boldsymbol{r}^i$ orthogonal to the column span of $\boldsymbol{V}^i$*

Proof. Let $\Delta \boldsymbol{r}^i$ be orthogonal to $\boldsymbol{V}^i$. Then, the components of the decomposition in iteration i are given by

$$\boldsymbol{c}^i = \arg\min_{\boldsymbol{c}^i} \|\Delta \boldsymbol{r}^i - \boldsymbol{V}^i \boldsymbol{c}^i\|_2 = [0 \ \dots \ 0]^T$$

$$\begin{aligned}
\Delta \boldsymbol{X}^i &= \boldsymbol{W}^i \boldsymbol{c}^i - \Delta \boldsymbol{r}^i \\
&= \boldsymbol{0} - \Delta \boldsymbol{r}^i \\
&= \boldsymbol{r}^i
\end{aligned}$$

Here, iteration i ends up as a fixed point iteration (see step 13 in Algorithm 2.1)

$$\boldsymbol{X}^{i+1} = \boldsymbol{X}^i + \boldsymbol{r}^i = \tilde{\boldsymbol{X}}^i$$

□

Algorithm 2.4 (QN-ILS BDM)**.** *Quasi-Newton algorithm with an approximation for the inverse of the Jacobian from a least-squares model to recover the zero-pressure geometry and the in vivo stress tensor field.*

1: $i = 0$
2: *Initialize* $\boldsymbol{X}^0 = \boldsymbol{x}_m$
3: $\boldsymbol{U}^0 = \mathcal{S}_U(\boldsymbol{X}^0)$
4: $\tilde{\boldsymbol{X}}^0 = \mathcal{B}(\boldsymbol{U}^0)$
5: $\boldsymbol{r}^0 = \tilde{\boldsymbol{X}}^0 - \boldsymbol{X}^0$
6: $\boldsymbol{X}^1 = \boldsymbol{X}^0 + \omega \boldsymbol{r}^0$
7: ***while*** $r_{rel}^i \geq \epsilon$ ***do***

$i = i + 1$
$\Omega(\boldsymbol{x}^i, \boldsymbol{\sigma}^i) = \mathcal{S}(\Omega(\boldsymbol{X}^i), p_m)$
$\boldsymbol{U}^i = \mathcal{S}_U(\boldsymbol{X}^i) = \boldsymbol{x}^i - \boldsymbol{X}^i$
$\tilde{\boldsymbol{X}}^i = \mathcal{B}(\boldsymbol{U}^i) = \boldsymbol{x}_m - \boldsymbol{U}^i$
$\boldsymbol{r}^i = \tilde{\boldsymbol{X}}^i - \boldsymbol{X}^i$
Construct $\boldsymbol{V}^i$ *and* $\boldsymbol{W}^i$ *as shown in Equation* (20a) *and* (22a)
Calculate QR-decomposition $\boldsymbol{V}^i = \boldsymbol{Q}^i \boldsymbol{R}^i$
Solve $\boldsymbol{R}^i \boldsymbol{c}^i = -{\boldsymbol{Q}^i}^T \boldsymbol{r}^i$
$\boldsymbol{X}^{i+1} = \boldsymbol{X}^i + \Delta \boldsymbol{X}^i = \boldsymbol{X}^i + \boldsymbol{W}^i \boldsymbol{c}^i + \boldsymbol{r}^i$
end while
Zero-pressure reference geometry $\boldsymbol{X}^* = \boldsymbol{X}^i$
In vivo stress tensor for the in vivo measured geometry $\boldsymbol{\sigma}^* = \boldsymbol{\sigma}^i$

Remark 2.5. Information from the previous backward displacement iterations is needed to calculate the approximation for the inverse of the Jacobian with the vector $-\boldsymbol{r}^i$. Therefore a relaxation with factor ω is performed in the first backward displacement iteration $i = 0$. As the same initial guess ($\boldsymbol{X}^0 = \boldsymbol{x}_m$) was made before when performing the backward displacement method using simple fixed point iterations, the values for the first two relative residuals, found by both methods, will be the identical when $\omega = 1$.

Remark 2.6. Definitions from section 2.2.1 and associated solving procedures in sections 2.2.2 and 2.2.3 can be reformulated in order to solve the inverse problem in function of the displacement. Here, a tilde is introduced to distinguish between the output variable of $\mathcal{S}_U(\mathcal{B}(U))$ and its input variable. The fixed point problem can be described by

$$\begin{aligned} \tilde{\boldsymbol{U}} &= \mathcal{S}_U(\mathcal{B}(\boldsymbol{U})) \\ &= \boldsymbol{U} = \boldsymbol{U}^* \end{aligned}$$

while the corresponding root finding formulation becomes

$$\mathcal{R}_U(\boldsymbol{U}) = \mathcal{S}_U \mathcal{B}(\boldsymbol{U})) - \boldsymbol{U} = \tilde{\boldsymbol{U}} - \boldsymbol{U} = \boldsymbol{0}$$

with $\mathcal{R}_U$ the residual operator in function of the displacement.

When solving for the zero-pressure configuration using Algorithm 2.1 or 2.4 the only variables which get updated explicitly are the material coordinates of the approximate zero-pressure geometry $\boldsymbol{X}^i$. However, the fixed point or root finding problem can perfectly be described in terms of $\boldsymbol{U}$ instead of $\boldsymbol{X}$. Moreover, both representations of the inverse problem yield the same theoretical result but with an opposite sign, as shown here for the root finding formulation

$$\begin{aligned} \mathcal{R}_U(\boldsymbol{U^i}) = \tilde{\boldsymbol{U}}^i - \boldsymbol{U}^i &= \mathcal{S}_U(\mathcal{B}(\boldsymbol{U}^i)) - \boldsymbol{U}^i && \text{(29a)} \\ &= \mathcal{S}_U(\boldsymbol{X}^i) - (\boldsymbol{x}_m - \boldsymbol{X}^i) && \text{(29b)} \\ &= \boldsymbol{X}^i - \mathcal{B}(\mathcal{S}(\boldsymbol{X}^i)) = -(\tilde{\boldsymbol{X}}^i - \boldsymbol{X}^i) = -\mathcal{R}_X(\boldsymbol{X}^i) && \text{(29c)} \end{aligned}$$

where Equations (29b) and (29c) are found by using the definition of the backward displacement function $\mathcal{B}$. $\mathcal{R}_U$ denotes the residual operator in function of the nodal displacement.

2.3. Existing solution methods and limitations

Besides the backward displacement method, proposed in this paper, there exist other techniques to incorporate in vivo stress into computational models of the cardiovascular system, given the in vivo image-based geometry $\boldsymbol{x}_m$ and the internal pressure load at the moment of image acquisition p_m.

The idea to take the zero-pressure geometry into account in a non-invasive way in the numerical modelling process of a blood vessel was first implemented by Raghavan et al. [16]. Their method can be described as an optimization procedure for finding the parameter k that approximates the coordinates of the unknown zero-pressure reference geometry $\boldsymbol{X}^*$ by $(\boldsymbol{x}_m - k\boldsymbol{U})$. Here, the nodal displacements $\boldsymbol{U}$ result from a single forward calculation where the lumen pressure load is applied onto the in vivo measured reference geometry $\boldsymbol{x}_m$.

The inverse elastostatic method as described by Govindjee and Mihalic [9] and later extended by the same authors for nearly incompressible materials [10] was introduced to the field of cardiovascular modelling by Lu et al. as another way to calculate the zero-pressure state [4]. However, the implementation involves access to the finite element code, what can be seen as a drawback.

Gee et al. implemented previous strategy as the Inverse Design (ID) method, and compared this prestressing technique with another method, the so called Modified Updated Lagrangian Formulation (MULF) [6, 17]. The methodology used, is similar to the Backward Incremental (BI) method introduced by de Putter et al. [5]. In contrast to the backward displacement method, described in this paper, the zero-pressure geometry is not calculated directly but the equilibrium configuration $\Omega(\boldsymbol{x}_m, \boldsymbol{\sigma}^*)$ is computed instead. By incrementally increasing the pressure load towards the full in vivo pressure p_m while discarding the corresponding deformations ($\boldsymbol{x}^i = \boldsymbol{x}_m$) a prestressed ($\boldsymbol{\sigma}^*$) and prestrained configuration is generated. The procedure calculates the new stress tensor field $\boldsymbol{\sigma}^i$ that will be used at the next increment by loading the i^{th} non-equilibrium configuration $\Omega(\boldsymbol{x}_m, \boldsymbol{\sigma}^{i-1})$ with the incrementally increased internal pressure ($p^i = p^{i-1} + \delta p^i$). As such, the stress tensor gets updated towards the in vivo stress tensor and the strain tensor gets implicitly updated by a multiplicative split of the deformation gradient tensor $\boldsymbol{F}_{0,i} = \boldsymbol{F}_{0,i-1}.\boldsymbol{F}_{i-1,i}$ [7, 18]. Afterwards, the zero-pressure geometry can be constructed by reducing the luminal pressure to 0 Pa [19]. According to [5] the last pressure increment has to be chosen extremely small to return a final equilibrium configuration. The method allows the use of a black box structural solver if the finite element code is able to update the initial stress tensor field with each iteration [19]. A similar approach of prestressing was used earlier by Pinsky et al. to include the internal stress state in the cornea under the presence of the full intraocular pressure load through a fixed point iteration instead of increasing the pressure incrementally [20].

Although the above methods only involve a structural model of the arterial system under consideration, their resulting zero-pressure geometry or in vivo stress state can also be used in FSI models, which take into account the interaction between the blood flow and the arterial wall, as the effect of viscous forces would be small. However, Bazilevs et al. report that the effect is not negligible [21] and account for the viscous traction caused by the fluid when solving the balance of linear momentum for the solid. They obtain the fluid traction vector from a separate steady flow CFD simulation with rigid walls. The prestress component $\boldsymbol{S}_0$ of the additive decomposition $(\boldsymbol{S} + \boldsymbol{S}_0)$ of the second Piola-Kirchhoff stress tensor is then calculated iteratively and used afterwards as initial stress in their in vivo geometry based FSI model [22].

3. Examples

This section focuses on two examples. In the first example a simplified model of a small artery is used for validation purpose and to evaluate the importance of stress incorporation in the in vivo measured geometry. The second example concerns a mouse-specific abdominal aorta with four side branches to explore the ability of the backward displacement method to restore a more complex cardiovascular structure at its zero-pressure state.

Both examples cover the comparison of the convergence resulting from the fixed point method and the quasi-Newton method with an approximation of the Jacobian's inverse from a least-squares model. All structural calculations were performed using the commercial finite element analysis software Abaqus/Standard (Simulia). However, as stated earlier, any other structural mechanics solver can be used.

3.1. **Example 1: In vivo stress incorporation in a thick-walled cylinder**

A small unloaded artery is modelled using a straight cylindrical tube with a length of 10 mm, an inner radius of 0.5 mm and a wall thickness to diameter ratio of 0.15. The boundary conditions only allow a radial displacement at the ending cross sections. The geometrical model is discretized using $64 \times 32 \times 4$ quadratic hexahedral elements with reduced integration and a hybrid formulation. The vessel wall behaviour is modelled by an incompressible isotropic hyperelastic material using the polynomial strain energy density function

$$W = C_{10}(I_1 - 3) + C_{01}(I_2 - 3) + C_{20}(I_1 - 3)^2 + C_{11}(I_1 - 3)(I_2 - 3) \tag{30}$$

where I_1 and I_2 are the first and the second invariant of the left Cauchy-Green deformation tensor, and where C_{ij} are empirically determined material constants for a human artery according to [23].

3.1.1. *Numerical validation of the backward displacement method*

To validate the backward displacement method a zero-pressure geometry is pressurized in a forward analysis by applying a uniformly distributed pressure load of 80 mmHg to the inner surface of the vessel wall. The resulting geometry is taken as the in vivo measured geometry at the diastolic phase and serves as a starting point for the backward problem. This inverse problem is then solved using the backward displacement method in order to restore a zero-pressure geometry which is eventually compared to the original zero-pressure geometry. Therefore, the residual vector $\boldsymbol{r}^i \in \mathbb{R}^{3N\times 1}$ is reshaped into the distance vector $\boldsymbol{d}^i \in \mathbb{R}^{N\times 3}$. Then, the error that is still present after iteration i can be defined as the mean distance between the nodes of the original image-based geometry $\boldsymbol{x}_m$ and the corresponding nodes of the i^{th} deformed geometry $\boldsymbol{x}^i$.

$$d^i_{mean} = \frac{1}{N}\sum_{j=1}^{N} \|\boldsymbol{d}^i_j\|_2$$

with $\boldsymbol{d}^i_j$ row j of matrix $\boldsymbol{d}^i$. Upon convergence, the in vivo measured geometry is fully recovered, with a mean distance error d^i_{mean} which is more than a factor 10^4 lower than the convergence criterion.

The evolution of the relative residual (15) throughout the iterative process is shown on a logarithmic scale in Figure 5 for both FP and QN-ILS iterations. This allows evaluation of the rate of convergence, when solving for the zero-pressure geometry, using the backward displacement method. For a convergence criterion set at e.g. 10^{-4}, the logarithm of the relative residual decreases linearly during consecutive iterations of the fixed point method. The quasi-Newton residuals however, reduce about one and a half times faster. As the additional cost of the QR-factorization is small compared to the cost of one forward calculation performed by the structural solver, the QN-ILS strategy can be used to accelerate the backward displacement method.

3.1.2. *Evaluation of the effect of in vivo stress incorporation*

To evaluate the effect of in vivo stress incorporation, a simulation is performed in which the internal pressure is first set to the end-diastolic pressure (80 mmHg) and subsequently increased to the end-systolic pressure (120 mmHg). This is done for three different set-ups:

(1) The in vivo measured geometry is assumed to be the unloaded geometry. In the forward simulation the in vivo measured geometry is inflated using the physiological pressure values (80 mmHg diastolic pressure; 120 mmHg systolic pressure). The results are visualized in quadrant I.
(2) The in vivo measured geometry is assumed to be the geometry at end-diastole, but neglects the existence of prestress at the diastolic phase. In the forward simulation the in vivo measured geometry is only inflated to 40 mmHg, the end-systolic minus end-diastolic pressure difference. To allow for a fair comparison of the calculated stresses with the other two cases, the stress tensor field was corrected, adding an approximation of the stress field at diastole. The latter resulted from a simulation in which 80 mmHg was applied onto the diastolic geometry. The results are visualized in quadrant IV.

(3) The proposed strategy in which the forward simulation towards the physiological pressure values starts from the restored zero-pressure geometry. This results in a prestressed in vivo geometry at diastole. The results are visualized in both quadrant II and III.

Figure 3(a) presents the maximum principal or circumferential stress at end-systole (120 mmHg). The contour plots are shown on the undeformed geometries from which the forward analysis was started. Figure 3(b) visualizes the radial displacement when the internal pressure load is increased from end-diastolic to end-systolic pressure. The red line and the grey dashed line are outlines of the corresponding deformed geometries. Note that the red outline of the diastolic geometry in quadrant IV coincides with the undeformed geometry.

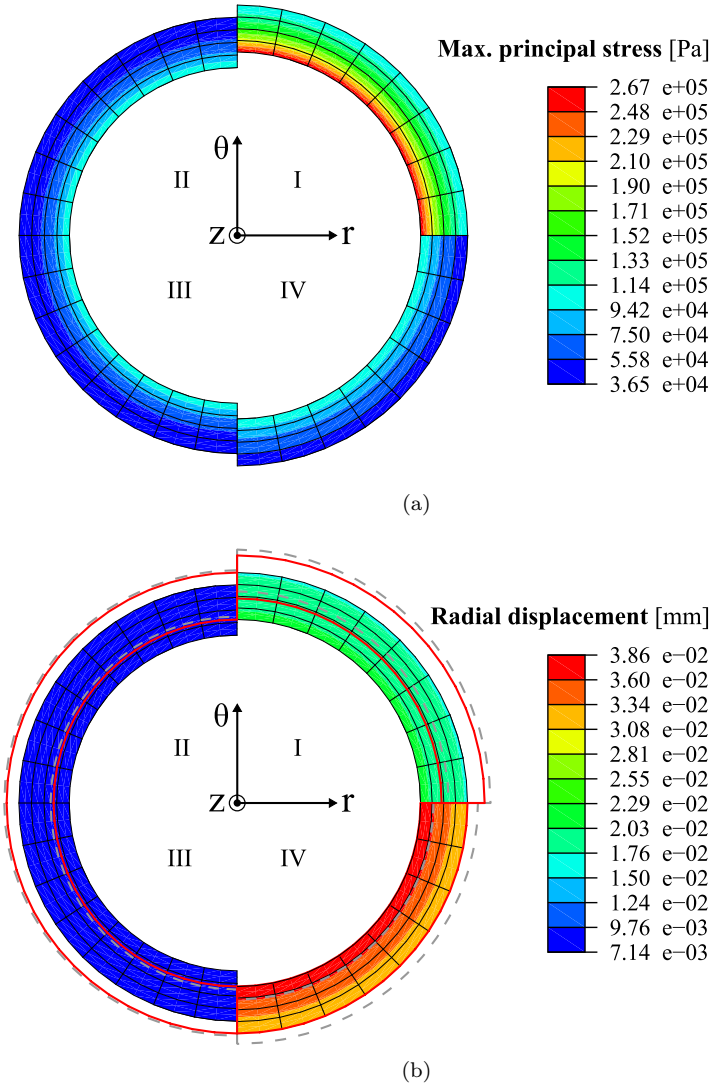

FIGURE 3. Contours of (a) the max. principal stress [Pa], and (b) the distance map between the geometries at end-diastole and end-systole [mm]. For more information about the different quadrants the reader is referred to the corresponding text in section 3.1.2.

Compared to quadrant II and III, the results in Figure 3(a) clearly show the overestimation of the maximum principal stress when the in vivo measured geometry is assumed to be the unloaded geometry (quadrant I). Furthermore, the outlines of the cross sectional areas at end-diastole and end-systole are a better approximation when the in vivo geometry is assumed to be the geometry at diastole (quadrant IV). However, the corresponding displacement contours in quadrant IV are overestimated due to the nonlinear material law and the absence of prestress and prestrain at the start of the inflation process.

3.2. **Example 2: In vivo stress incorporation in a mouse-specific abdominal aorta**

In a second example, a more complex cardiovascular structure was created based on contrast-enhanced micro-CT images of the abdominal aorta of an in-house bred male ApoE -/- mouse on a C57BL/6 background (age: 5 months, body weight: 29 g). A mouse-specific 3D geometry of the aortic lumen containing four side branches was obtained in vivo, by segmentation of micro-CT (Triumph, Gamma Medica) images in Mimics (Materialise). In order to obtain sufficient contrast during the imaging process the mouse was intravenously injected with Aurovist (Nanoprobes), a contrast agent which provided satisfying results in earlier studies [1]. Using pyFormex [24] a structured grid was projected onto the from segmentation resulting outer surface yielding a hexahedral mesh for the aortic wall, Figure 4(a), according to the method of De Santis et al. [25]. The mesh for the aortic wall consists of 80640 elements with 5 elements to represent the wall thickness, 48 elements in the circumferential direction and local refinements in the bifurcation regions, Figure 4(b). The wall thickness was assumed to be 20 percent of the local radius and thus varies throughout the structure.

The element type, the free radial displacement boundary condition at the ending cross sections (3) and the polynomial hyperelastic material model (30) were adopted from the first example (section 3.1). For example purpose only, identical material parameters as in the example of the human vessel were used for the constitutive material law.

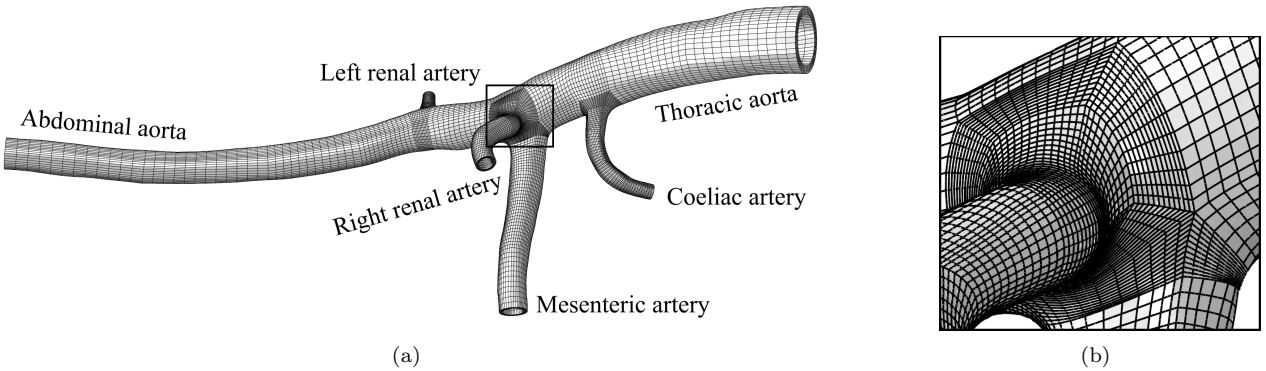

FIGURE 4. Hexaedral mesh for the arterial wall of the abdominal aorta of a mouse (length sample about 20 mm) and its side branches (a), and a detail of the mesh at the trifurcation region (b).

To further evaluate the backward displacement method this more complex geometry was brought to its zero-pressure state, assuming the internal pressure load at the moment of medical imaging to be 80 mmHg. Afterwards, in vivo stress was computed by reapplying this pressure load in a forward calculation.

The rate of convergence is plotted for backward displacement simulations using both the fixed point and the quasi-Newton approach, Figure 5. In comparison with the fixed point convergence rate of the simplified artery in example 1, the logarithm of the relative residual now follows a linear decline after the second iteration. Although the geometry is much more complicated, a convergence criterion set at e.g. 10^{-4} would slow down the convergence only 3.33 (FP) and a 2.75 (QN-ILS) times. The quasi-Newton approach returns a converged

solution twice as fast and thus shows an even more significant acceleration of the backward displacement method when using a complex geometry. Remark that the wall clock time of the overall calculation varies linearly with the number of iterations. The proportionality constant is the time required to perform one forward calculation.

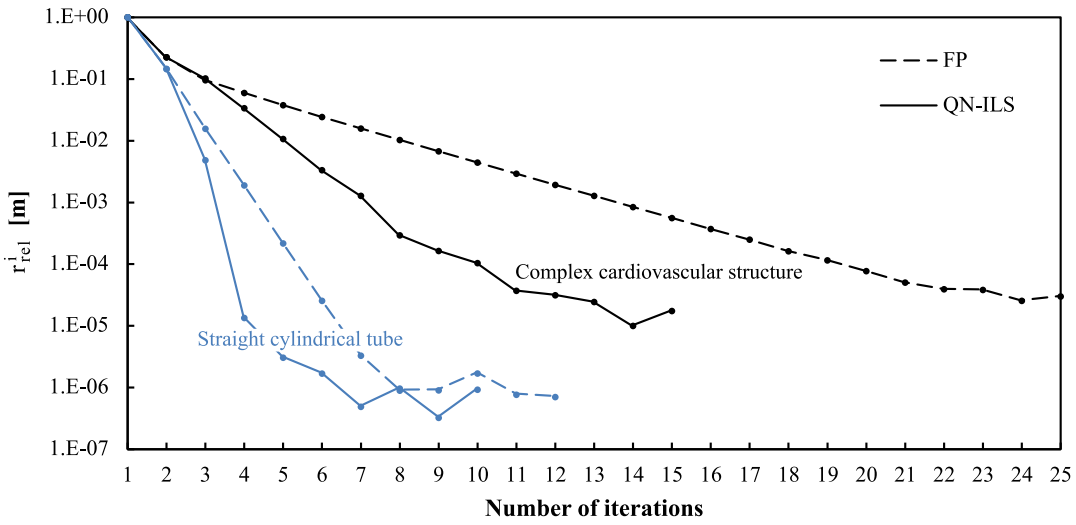

FIGURE 5. Rate of convergence when solving for the zero-pressure geometry of a thick-walled cylinder (example 1) and a mouse-specific abdominal aorta (example 2) using the backward displacement method. Results are shown for both the fixed point (FP) and the quasi-Newton (QN-ILS) approach.

Figure 6 depicts the contour plots of the maximum principal stress and the displacement field present in the in vivo measured geometry at the moment of medical imaging. This is the result of applying the end-diastolic pressure on the restored zero-pressure geometry of the more complex cardiovascular structure.

4. Conclusion

In conclusion, this paper presents a method to restore the original geometry of a structure in absence of its loading state, and to recover the stress field of the final, loaded structure. This inverse problem can be formulated using a backward displacement function and a function which represents the outcome of the structural solver. To solve this backward displacement problem, a fixed point algorithm and a quasi-Newton algorithm are proposed in sections 2.2.2 and 2.2.3. The backward displacement method is validated in section 3.1.1, concluding that it is ideally suited to restore the zero-pressure geometry of in vivo measured cardiovascular structures (section 3.2). To emphasize the importance of prestress in this field of research, the example in section 3.1 shows that incorporation of in vivo stress in arteries is necessary to properly estimate stress and displacement in the physiological blood pressure range. The convergence rate of the proposed techniques is high and decreases only slightly for a much more complex structure using the same constitutive material law. Furthermore, the convergence rate of the fixed point iterative strategy is compared to the quasi-Newton algorithm with a least-squares approximation for the inverse of the Jacobian. As shown in Figure 5, the use of information from previous iterations, as is done in the QN-ILS algorithm, accelerates the backward displacement method significantly. Finally and most importantly, the backward displacement method allows for a straightforward implementation of the algorithm in combination with existing structural solvers as only an update of the coordinates of the mesh needs to be performed.

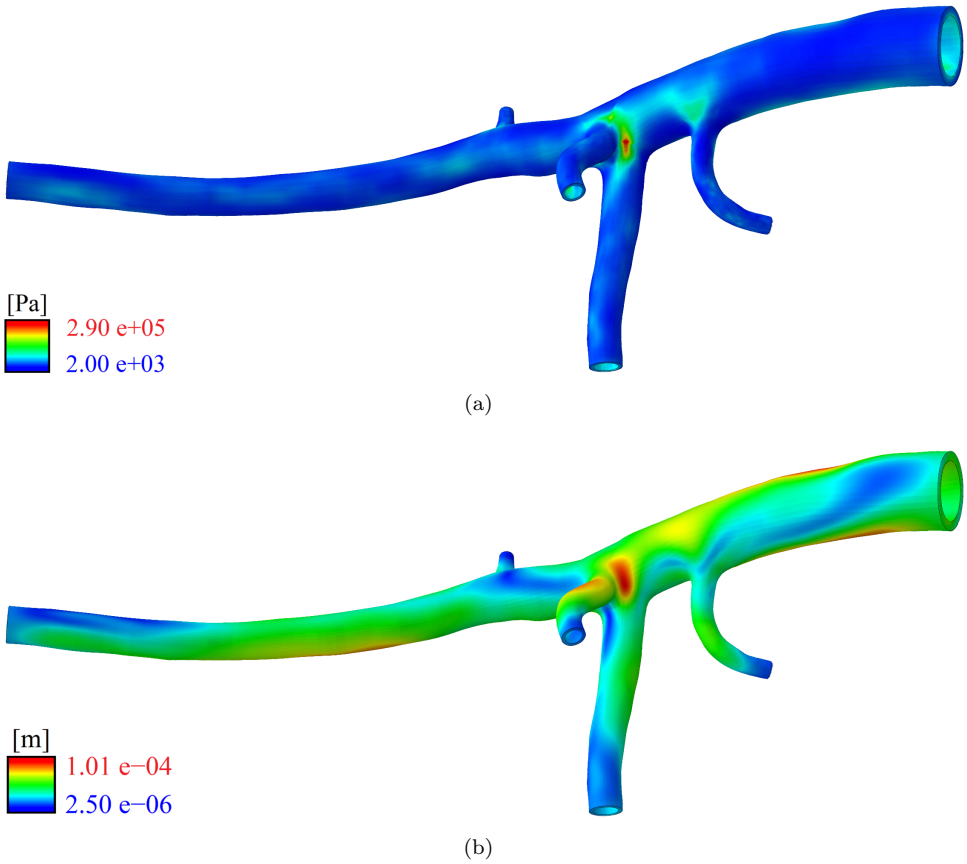

FIGURE 6. Contours of (a) the max. principal stress [Pa], and (b) the displacement [m]. Both after applying the internal pressure load, present at the moment of medical imaging, onto the restored zero-pressure geometry.

ACKNOWLEDGMENTS

This research was funded by the Special Research Fund of the Ghent University (BOF10/GOA/005) and by the Research Foundation - Flanders (FWO) project nr. G.0275.08. Joris Degroote gratefully acknowledges funding by a post-doctoral fellowship of the Research Foundation - Flanders (FWO). Bram Trachet is recipient of a research grant of the Flemish government agency for Innovation by Science and Technology (IWT).

REFERENCES

[1] B. Trachet, M. Renard, G. De Santis, S. Staelens, J. De Backer, L. Antiga, B. Loeys, and P. Segers. An integrated framework to quantitatively link mouse-specific hemodynamics to aneurysm formation in angiotensin II-infused ApoE -/- mice. *Annals of Biomedical Engineering*, 39:2430–2444, 2011.

[2] H. J. Kim, I. E. Vignon-Clementel, C. A. Figueroa, J. F. LaDisa, K. E. Jansen, J. A. Feinstein, and C. A. Taylor. On coupling a lumped parameter heart model and a three-dimensional finite element aorta model. *Annals of Biomedical Engineering*, 37:2153–2169, 2009.

[3] J. Degroote, I. Couckuyt, J. Vierendeels, P. Segers, and T. Dhaene. Inverse modelling of an aneurysms stiffness using surrogate-based optimization and fluid-structure interaction simulations. *Structural and Multidisciplinary Optimization*, pages 1–13, 2012.

[4] J. Lu, X. Zhou, and M. L. Raghavan. Inverse elastostatic stress analysis in pre-deformed biological structures: Demonstration using abdominal aortic aneurysms. *Journal of Biomechanics*, 40(3):693–6, 2007.
[5] S. de Putter, B. J. B. M. Wolters, M. C. M. Rutten, M. Breeuwer, F. A. Gerritsen, and F. N. van de Vosse. Patient-specific initial wall stress in abdominal aortic aneurysms with a backward incremental method. *Journal of Biomechanics*, 40(5):1081–1090, 2007.
[6] M W Gee, C Reeps, H H Eckstein, and W A Wall. Prestressing in finite deformation abdominal aortic aneurysm simulation. *Journal of Biomechanics*, 42:1732–1739, 2009.
[7] L. Speelman, E. M. H. Bosboom, G.W.H. Schurink, J. Buth, M. Breeuwer, M.J. Jacobs, and F.N. van de Vosse. Initial stress and nonlinear material behavior in patient-specific AAA wall stress analysis. *Journal of Biomechanics*, 42(11):1713 – 1719, 2009.
[8] M.A.G. Merkx, M. van 't Veer, L. Speelman, M. Breeuwer, J. Buth, and F.N. van de Vosse. Importance of initial stress for abdominal aortic aneurysm wall motion: Dynamic MRI validated finite element analysis. *Journal of Biomechanics*, 42(14):2369 – 2373, 2009.
[9] S. Govindjee and P. A. Mihalic. Computational methods for inverse finite elastostatics. *Computer Methods in Applied Mechanics and Engineering*, 136(1-2):47 – 57, 1996.
[10] S. Govindjee and P. A. Mihalic. Computational methods for inverse deformations in quasi-incompressible finite elasticity. *International Journal for Numerical Methods in Engineering*, 43(5):821–838, 1998.
[11] V. D. Fachinotti, A. Cardona, and P. Jetteur. Finite element modelling of inverse design problems in large deformations anisotropic hyperelasticity. *International Journal for Numerical Methods in Engineering*, 74(6):894–910, 2008.
[12] R. Haelterman, J. Degroote, D. Van Heule, and J. Vierendeels. The quasi-newton least squares method: A new and fast secant method analyzed for linear systems. *SIAM Journal on Numerical Analysis*, 47(3):2347–2368, 2009.
[13] J. Degroote, KJ. Bathe, and J. Vierendeels. Performance of a new partitioned procedure versus a monolithic procedure in fluid-structure interaction. *Computers and Structures*, 87:793–801, June 2009.
[14] R. Haelterman, J. Degroote, D. Van Heule, and J. Vierendeels. On the similarities between the quasi-newton inverse least squares method and GMRes. *SIAM Journal on Numerical Analysis*, 47(6):4660–4679, 2010.
[15] J. Degroote, R. Haelterman, S. Annerel, P. Bruggeman, and J. Vierendeels. Performance of partitioned procedures in fluid-structure interaction. *Computers and Structures*, 88:446–457, April 2010.
[16] M. L. Raghavan, B. Ma, and M. Fillinger. Non-invasive determination of zero-pressure geometry of arterial aneurysms. *Annals of Biomedical Engineering*, 34:1414–1419, 2006.
[17] M. W. Gee, Ch. Förster, and W. A. Wall. A computational strategy for prestressing patient-specific biomechanical problems under finite deformation. *International Journal for Numerical Methods in Biomedical Engineering*, 26(1):52–72, 2010.
[18] V. Alastrué, A. Garía, E. Peña, J. F. Rodríguez, M. A. Martínez, and M. Doblaré. Numerical framework for patient-specific computational modelling of vascular tissue. *International Journal for Numerical Methods in Biomedical Engineering*, 26(1):35–51, 2010.
[19] L. Speelman, A. C. Akyildiz, B. den Adel, J. J. Wentzel, A. F. W. van der Steen, R. Virmani, L. van der Weerd, J. W. Jukema, R. E. Poelmann, E. H. van Brummelen, and F. J. H. Gijsen. Initial stress in biomechanical models of atherosclerotic plaques. *Journal of Biomechanics*, 44(13):2376 – 2382, 2011.
[20] P. M. Pinsky, D. van der Heide, and D. Chernyak. Computational modeling of mechanical anisotropy in the cornea and sclera. *Journal of cataract and refractive surgery*, 31(1):136–45, 2005.
[21] Y. Bazilevs, M. C. Hsu, Y. Zhang, W. Wang, T. Kvamsdal, S. Hentschel, and J. Isaksen. Computational vascular fluid-structure interaction: methodology and application to cerebral aneurysms. *Biomechanics and Modeling in Mechanobiology*, 9:481–498, 2010.
[22] M. C. Hsu and Y. Bazilevs. Blood vessel tissue prestress modeling for vascular fluid-structure interaction simulation. *Finite Elements in Analysis and Design*, 47:593–599, June 2011.
[23] P. J. Prendergast, C. Lally, S. Daly, A. J. Reid, T. C. Lee, D. Quinn, and F. Dolan. Analysis of prolapse in cardiovascular stents: A constitutive equation for vascular tissue and finite-element modelling. *Journal of Biomechanical Engineering*, 125(5):692–699, 2003.
[24] http://www.pyformex.org.
[25] G. De Santis, M. De Beule, K. Van Canneyt, P. Segers, P. Verdonck, and B. Verhegghe. Full-hexahedral structured meshing for image-based computational vascular modeling. *Medical Engineering & Physics*, 33(10):1318 – 1325, 2011.